Article
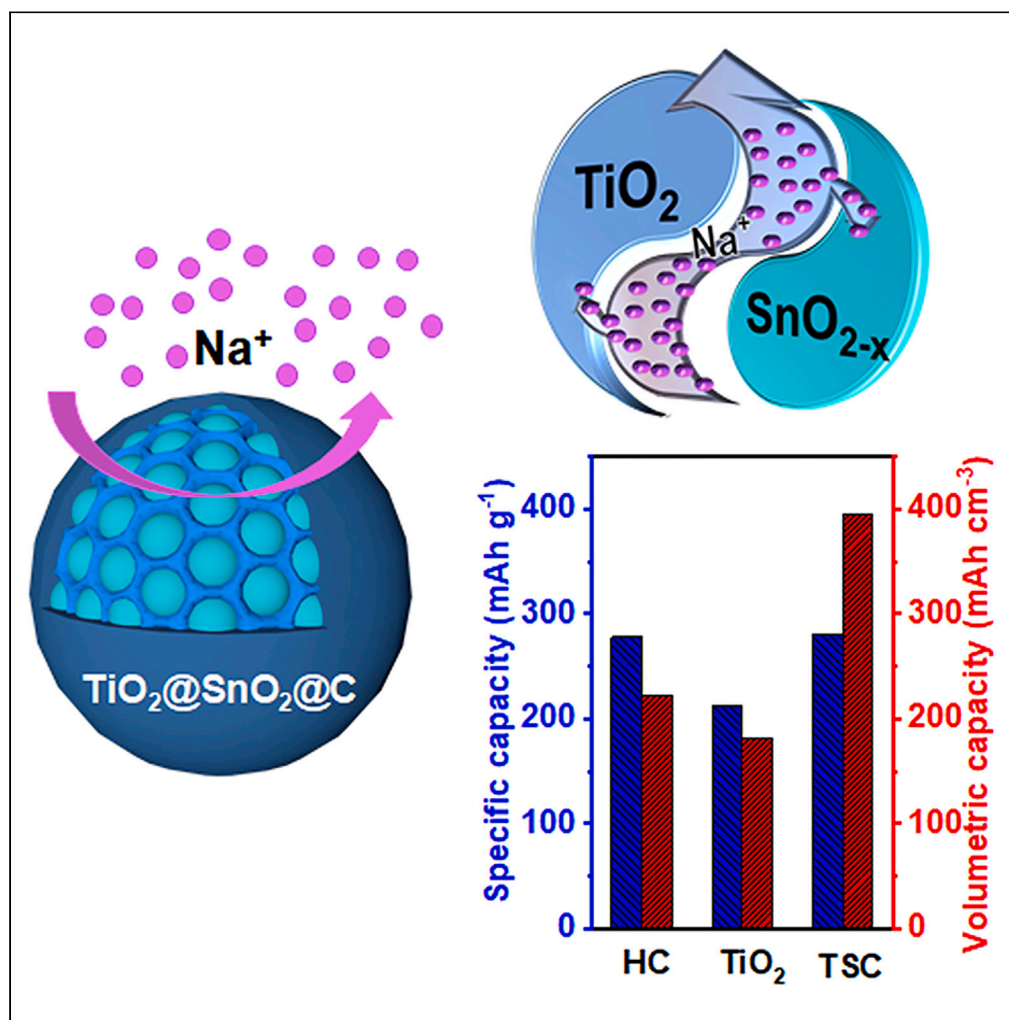
Compact TiO$_2$@SnO$_2$@C heterostructured particles as anode materials for sodium-ion batteries with improved volumetric capacity

Zhikun Hu, Zerui Chen, Qianqian Liu, Wei Zhao, Yifei Xu, Hao Bin Wu

hbwu@zju.edu.cn

Highlights

Compact heterostructured TiO$_2$@SnO$_2$@C particles are developed for efficient Na storage

Heterostructure between TiO$_2$ and SnO$_2$ promotes charge transfer and redox reaction

High volumetric capacity over porous TiO$_2$ and commercial hard carbon is demonstrated

Article

Compact TiO₂@SnO₂@C heterostructured particles as anode materials for sodium-ion batteries with improved volumetric capacity

Zhikun Hu,[1,3] Zerui Chen,[1,3] Qianqian Liu,[2] Wei Zhao,[1] Yifei Xu,[1] and Hao Bin Wu[1,4,*]

SUMMARY

Sodium-ion batteries (SIBs) are promising candidates for large-scale energy storage. Increasing the energy density of SIBs demands anode materials with high gravimetric and volumetric capacity. To overcome the drawback of low density of conventional nanosized or porous electrode materials, compact heterostructured particles are developed in this work with improved Na storage capacity by volume, which are composed of SnO_2 nanoparticles loaded into nanoporous TiO_2 followed by carbon coating. The resulted $TiO_2@SnO_2@C$ (denoted as TSC) particles inherit the structural integrity of TiO_2 and extra capacity contribution from SnO_2, delivering a volumetric capacity of 393 mAh cm^{-3} notably higher than that of porous TiO_2 and commercial hard carbon. The heterogeneous interface between TiO_2 and SnO_2 is believed to promote the charge transfer and facilitate the redox reactions in the compact heterogeneous particles. This work demonstrates a useful strategy for electrode materials with high volumetric capacity.

INTRODUCTION

With the increasing demand for the large-scale energy storage, sodium-ion batteries (SIBs) are becoming promising candidates due to the high abundance of sodium, low cost, and improved safety in comparison with lithium-ion batteries (LIBs).[1–8] However, the relatively low energy density of SIBs represents one of the major drawbacks toward the large-scale applications.[6,9] Over the past years, efforts have been made to develop advanced electrode materials for SIBs. For example, hard carbon has been widely employed as the anode material for commercialized SIBs in view of the reasonable cost and performance.[10–15] Nonetheless, the insufficient energy density and potential safety concern associating with the low sodium storage represent the major drawbacks of hard carbon anode,[16] which raises the urgency to develop alternative materials.

As a typical insertion anodes, TiO_2 has attracted much attention for its naturally abundance, non-toxicity, and easy preparation.[17–20] Excellent cycling stability and high-rate performance was demonstrated when employing anatase TiO_2 as the anode for SIBs,[21,22] which could be attributed to the prominent pseudocapacitive behavior of nanostructured TiO_2.[23] However, the specific capacity of TiO_2 has been generally limited to ca. 200 mAh g^{-1}, while the nanostructure feature further lowers the volumetric capacity.[24] Unlike most insertion anode, alloying and conversion anodes such as SnO_2 would potentially deliver much impressive specific capacity (e.g., theoretically 1378 mA h g^{-1} based on $SnO_2 + 7.75Na^+ + 7.75e^- \rightarrow Na_{3.75}Sn + 2Na_2O$).[25–30] However, the application of SnO_2 was restricted by its sluggish reaction kinetics and rapid capacity fading.[31–33]

Composite materials of TiO_2 and SnO_2 have been proposed to inherit the merits of each component. For instance, Liang et al.[34] fabricated one-dimensional tubular $SnO_2@TiO_2$ core-shell nanocomposites with slightly improved cycling stability. Yang et al.[35] construct a hollow paramecium-like $SnO_2@TiO_2$ delivering a limited capacity of 200 mA h g^{-1}. Tian et al.[36] reported $SnO_2@C@TiO_2$ hollow spheres with three-layer structure, delivering a high capacity of 381 mAh g^{-1} and improved stability. Despite certain improvement in specific capacity, these composite electrode materials possess porous or hollow structure to facilitate electrolyte penetration and accommodate volume expansion,[34–37] which obviously sacrificed the volume utilization and low volumetric energy density of active materials, limiting their use in practical SIBs.[38]

[1]Institute for Composites Science Innovation (InCSI) and State Key Laboratory of Silicon Materials, School of Materials Science and Engineering, Zhejiang University, Hangzhou 310027, P. R. China

[2]Key Laboratory of Electronic Materials and Devices of Tianjin, School of Electronics and Information Engineering, Hebei University of Technology, Tianjin, China

[3]These authors contributed equally

[4]Lead contact

*Correspondence:
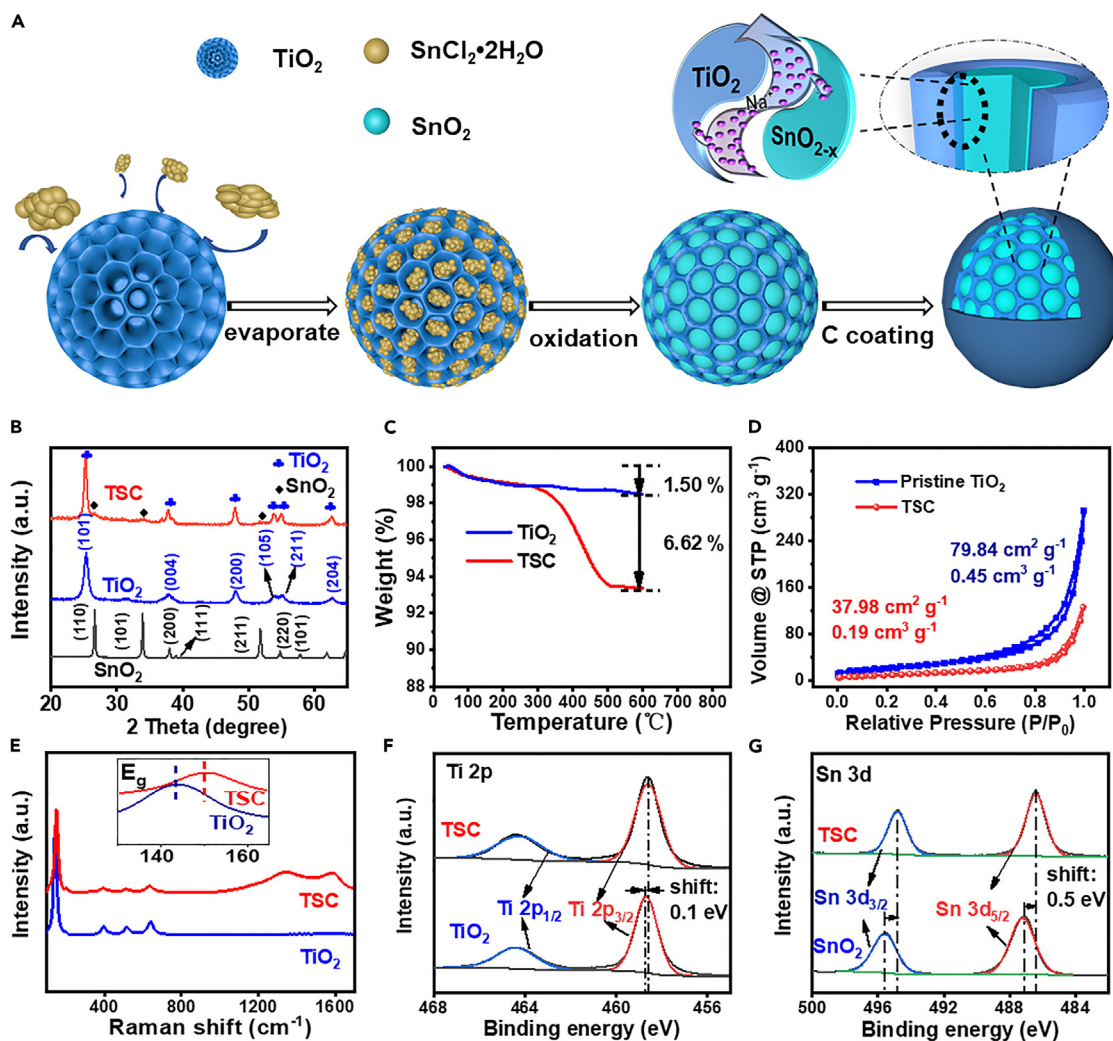hbwu@zju.edu.cn

https://doi.org/10.1016/j.isci.2023.106642

Figure 1. Synthesis and physical characterizations of TSC

(A) Schematics illustration of the synthesis of TSC.

(B) XRD pattern of TSC, pure TiO_2, and SnO_2.

(C) TGA profile of TSC and TiO_2.

(D) N_2 adsorption–desorption isotherms.

(E) Raman spectra of pristine TiO_2 and TSC.

(F) Ti 2p and (G) Sn 3d XPS spectra of TSC and TiO_2 or SnO_2.

In this work, compact heterogeneous particles composed of porous TiO_2 framework and confined SnO_2 have been demonstrated as anode materials for SIBs with improved volumetric capacity. We have previously shown that nonporous bulky particles with proper heterogeneous interface would possess notable interface-induced pseudocapacitance, leading to high volumetric capacity.[24] Herein, SnO_2 nanoparticles were loaded into nanoporous TiO_2, forming a compact heterostructure that inherits the structural integrity of TiO_2 and extra capacity contribution from SnO_2. Electrochemical analysis revealed the promoted charge transfer in the heterogeneous particles, which compensates the drawbacks brought by the extended charge transport length. As a result, the volumetric capacity of compact TiO_2/SnO_2 heterostructured particles was twice that of porous TiO_2 and even much higher than commercial hard carbon anode.

RESULTS AND DISCUSSION

Synthesis and structural characterization

The preparation of $TiO_2@SnO_2@C$ heterostructured particles was illustrated in Figure 1A. Porous TiO_2 spheres were synthesized by a previous reported method.[39] $SnCl_2·2H_2O$ was introduced into the

sub-micrometer porous TiO_2 spheres by a solvent evaporation method to obtain the $TiO_2@SnCl_2\cdot2H_2O$ precursor. After high-temperature treatment in air, Sn^{2+} was oxidized to Sn^{4+} to form TS. The content of SnO_2 in TS was about 20 wt % based on the feed ratio of the precursors. To improve the electronic conductivity and structural stability, a thin carbon layer was coated on the surface of the TS spheres by using dopamine as carbon source, which was named TSC.

Figure 1B showed the X-ray diffraction (XRD) patterns of the as-prepared TSC, TiO_2, and SnO_2 (Figure S1). The XRD pattern of TiO_2 showed peaks at 25°, 48°, and 37.8°, corresponding to the (101), (200), and (004) crystal planes,[21] respectively. SnO_2 showed peaks at about 26.6°, 33.8°, and 51.7°, corresponding to the (110), (101), and (211) crystal planes, respectively.[40] As for the XRD pattern of TSC, obvious peaks belonging to TiO_2 were observed. The poorly observed diffraction peaks belonging to SnO_2 resulted from the low crystallinity of SnO_2 confined in nanochannels.[41] Figure 1C shows the thermogravimetric analysis profile of TSC and TiO_2 under air. The weight loss about 1.50% from TiO_2 below 100°C was related to loss of the surface hydroxide groups and adsorbed moisture. The curve of TSC showed obvious weight loss of 6.62% between 300°C and 400°C, which results from the loss of carbon. The pore structure of TiO_2 and TSC was studied by nitrogen adsorption isotherms (Figure 1D). The specific surface area and pore volume of TiO_2 were about 79.84 $cm^2\ g^{-1}$ and 0.45 $cm^3\ g^{-1}$, which decreased to 37.98 $cm^2\ g^{-1}$ and 0.19 $cm^3\ g^{-1}$ after the introduction of SnO_2, respectively. These changes confirmed that the porous channels of TiO_2 particles were filled with SnO_2 to form a compact structure with low porosity.

Raman spectroscopy was performed to investigate the defective structures of different components in the TSC (Figure 1E). The Raman spectra of TiO_2 showed an obvious peak at about 143 cm^{-1}, which was contributed to the Ti-O bond. The corresponding peak of TSC shifted to a higher position, indicating crystal distortion and presence of defects.[42] The peaks at about 1350 and 1590 cm^{-1} resulted from a disorder-induced feature (D-band) and the E_{2g} mode of graphite (G-band), respectively (Figure S2A).[43] These peaks demonstrated the exitance of both graphitized and less-graphitized carbon. The X-ray photoelectron spectroscopic (XPS) test was performed to further investigate the surface chemical state of the TiO_2 and TSC (Figure S2B). For TSC, peaks of Ti 2p and Sn 3d both shifted to lower binding energy compared with pure TiO_2 and SnO_2 (shifted by −0.1 and −0.5 eV, respectively) as shown in Figures 1F and 1G. Similar Raman shift has been reported to arise from the electronic interaction at heterogeneous interface.[44–47] To exclude the effect of carbon layer, the Sn 3d XPS spectrum of TS was also carried out, showing similar results (Figure S2D). Meanwhile, the diffraction peak of TiO_2 for TSC also shifted to a lower degree in the XRD pattern (Figure S2E), suggesting the strong coupling and intimate contact between the TiO_2 and SnO_2.[48]

The morphology and nanostructure of porous TiO_2 spheres and TSC were studied by scanning electron microscope and transmission electron microscope (TEM). As shown in Figures 2A and 2B, the porous TiO_2 spheres exhibit a flower-like morphology assembled by sheet-like subunits with a thickness of around 10 nm. The disappearance of the large space between TiO_2 nanosheets confirmed the successful incorporation of SnO_2 to form the TS composite with a compact structure (Figures S3A and S3B). TSC nanoparticles with rough surface were synthesized by coating TS with carbon layer (Figures 2C and 2D). During the synthesis process, the size of sub-micrometer spheres was perfectly inherited.

TEM images demonstrated the nonporous texture of TSC, which confirmed the existence of SnO_2 inside porous TiO_2. The corresponding high-resolution TEM demonstrated lattice fringes belonging to the (101) crystal plane of anatase TiO_2 and the (200) crystal plane of SnO_2 (with lattice spacing of 0.357 and 0.237 nm, respectively) (Figures 2F and 2G). A carbon layer with thickness of about 2 nm could be observed (highlighted in Figure 2G). The diffraction rings belonging to the (101) crystal plane of TiO_2 and the (101) crystal plane of SnO_2 were also obtained by selected area electron diffraction. Meanwhile, the weak diffraction ring belonging to SnO_2 suggests the poor crystallinity, which was consistent with the XRD result. Elemental mappings by energy dispersive spectrometer indicated the uniform distribution of Ti, Sn, and C elements (Figure 2I), confirming the homogeneous loading of SnO_2 in the TiO_2 framework as well as the conformal coating of carbon layer. The absence of chloride element (Figure S4) confirms the complete conversion of $SnCl_2\cdot2H_2O$ precursor into SnO_2.

Characterization of electrochemical properties

The electrochemical sodium storage performance of TSC was systematically evaluated. Figures S5A and S5B showed the CV curve of TSC with voltage window of 0.01–2.5 V at 0.1 mV s^{-1} sweep rate. After the first cycle, the CV curves showed good repeatability, indicating the excellent reversibility of the electrochemical reaction. The
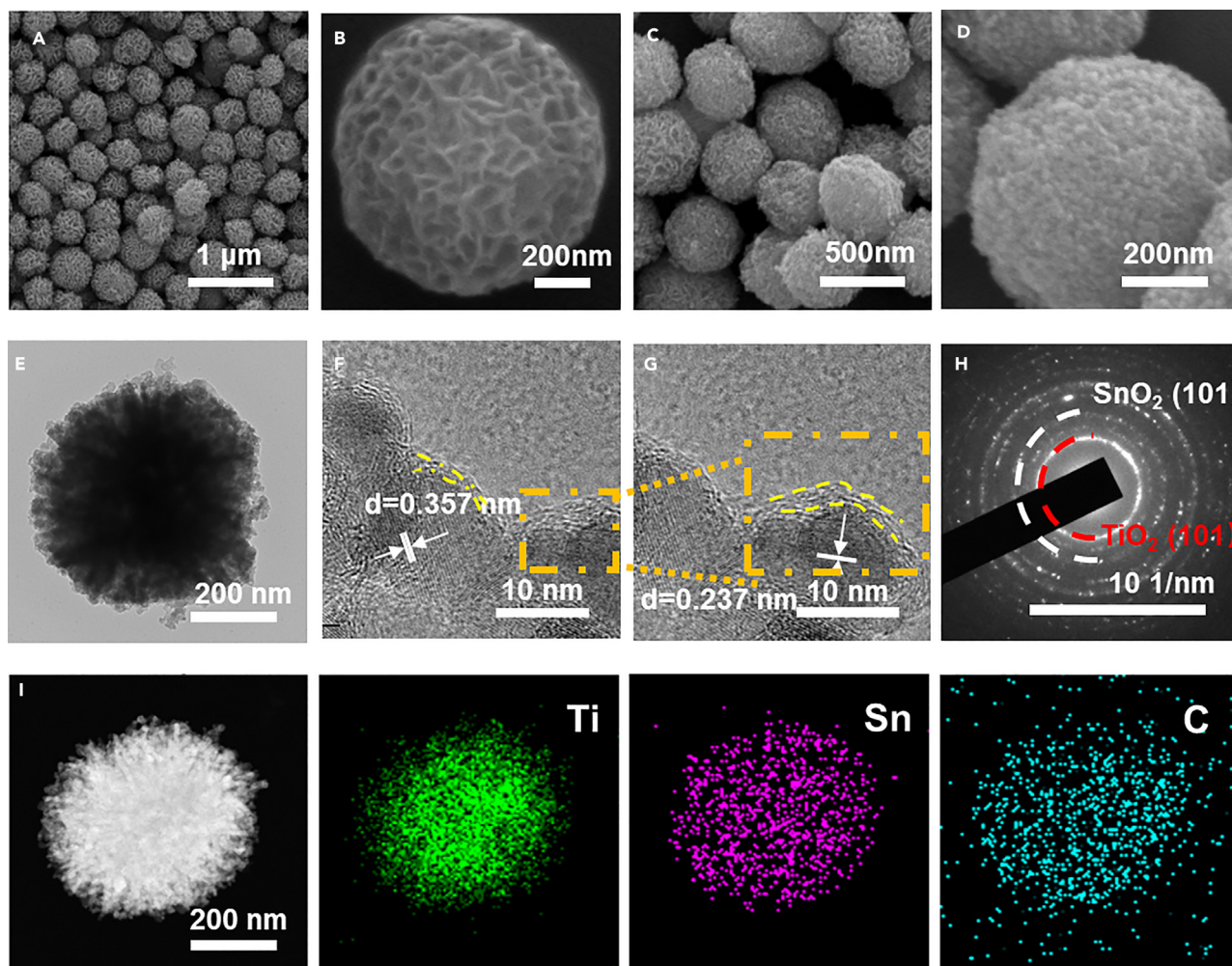
Figure 2. Morphological and microstructure characterizations of TSC
(A–D) SEM images of (A and B) pristine TiO$_2$ and (C and D) TSC.
(E) TEM.
(F and G) HRTEM images.
(H) SAED patterns of TSC.
(I) EDS elemental mappings of TSC.

peak at the voltage of 0.02 V during the first cycle was related to the decomposition of electrolyte and the formation of solid electrolyte interface (SEI). The reduction peak at 1.2–1.5 V was attributed to the reduction of SnO$_2$ into metallic Sn. The reduction peak at 0.2–1.3 V resulted from the insertion of Na$^+$ into TiO$_2$ and the alloy reaction of metallic Sn.[49,50] The oxidation peak at 0.6–1.3 V was attributed to the dealloying reaction to Sn and the de-sodiation of Na$_x$TiO$_2$, which were the inverse processes of the above reactions.[34,51]

Figures 3A and 3B showed the galvanostatic charge and discharge performance of TiO$_2$ and TSC. The discharge and charging-specific capacity of TiO$_2$ in the first cycle were 265 and 156 mAh cm^{-3}, respectively. TSC possessed much higher discharge and charging capacity (667 and 357 mAh cm^{-3}, respectively). The low initial Coulombic efficiency of TSC could be attributed to the formation of SEI and the irreversible conversion of SnO$_2$ into Sn. From the second cycle onward, the charge/discharge curves gradually stabilize. Note that the TSC only shows slightly improved reversible gravimetric capacity compared with TiO$_2$, yet the improvement in volumetric capacity is much pronounced (Figure S5C). As compared in Figure 3C, after incorporating high-capacity component (SnO$_2$) and inactive carbon layer, the gravimetric capacity increases from 208 mAh g^{-1} of pure nanoporous TiO$_2$ to 279 mAh g^{-1} of TSC. Given that the SnO$_2$ nanoparticles only occupy the inner cavity of nanoporous TiO$_2$, a significant increase of tap density was observed (1.39 and 0.88 g cm^{-3} for TSC and TiO$_2$,
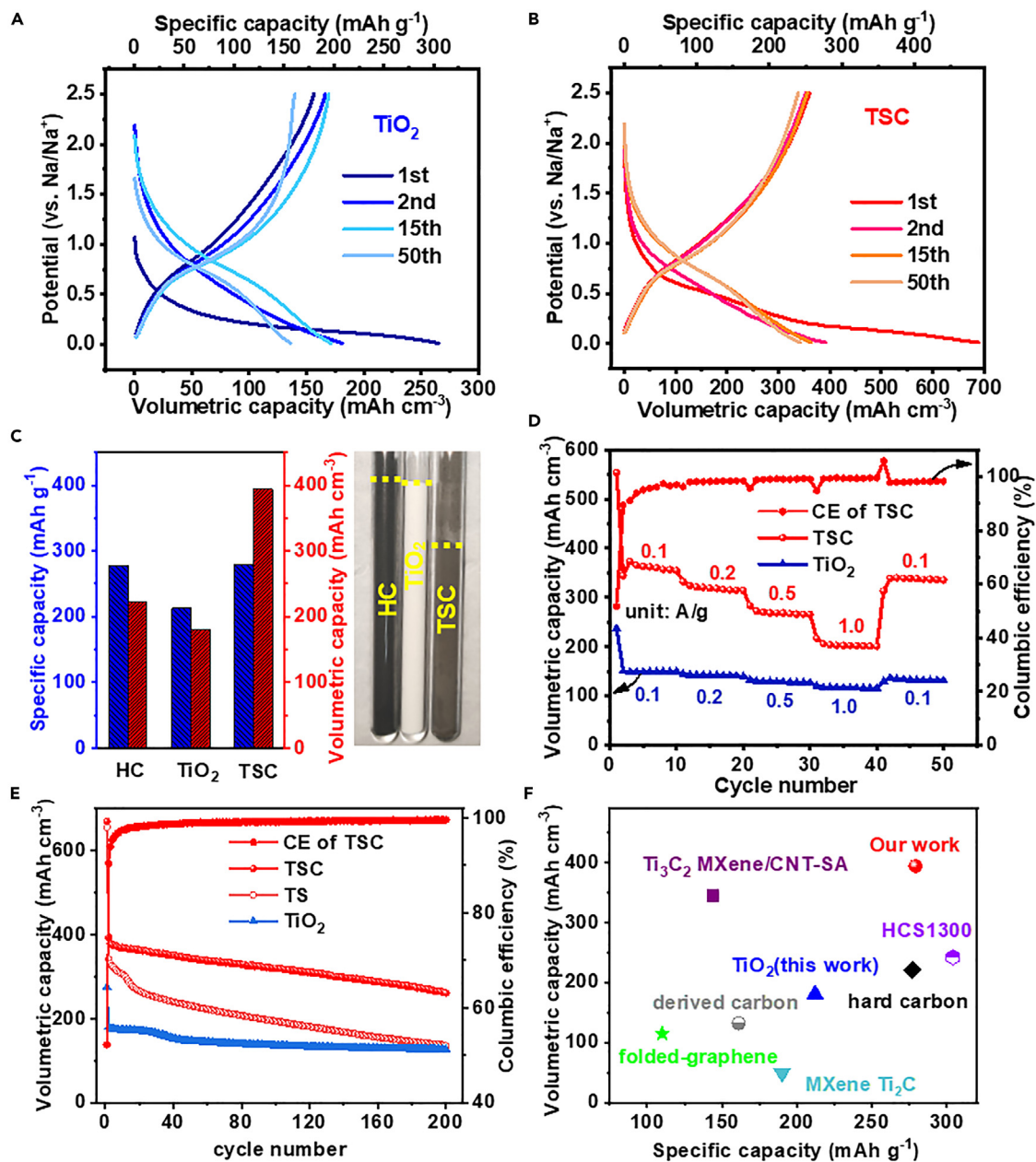
Figure 3. Electrochemical Na storage performance of TSC
(A and B) Typical discharge–charge voltage profiles of (A) TiO_2 and (B) TSC.
(C) Volumetric/specific capacity (left) and volume comparison of the same weight (right) of various electrode materials.
(D) Rate performances of TSC and TiO_2 at different current density.
(E) The cycling performance of TiO_2, TS, and TSC.
(F) Comparison of gravimetric/volumetric capacity of hard carbon (HC), TiO_2, TSC, and other reported anode materials. Volumetric capacity is estimated based on gravimetric capacity and tap density.

respectively). Collectively, the volumetric capacity of TSC (393 mAh cm^{-3}) is more than twice that of TiO_2 (181 mAh cm^{-3}), and much higher than that of commercial hard carbon (221 mAh cm^{-3}).

Figures 3D and S5D show the rate performance of TSC and TiO_2 at different current densities. When the current density was 0.1, 0.2, 0.5, 1.0, and 0.1 A g^{-1}, TSC nanoparticles maintained discharging capacities of 357, 326, 274, and 204 mAh cm^{-3}, respectively, which were much higher than that of TiO_2 (153.6,

145.0, 124.8, 107, and 134.6 mAh cm^{-3}, respectively). Though the compact structure of TSC might extend the diffusion path for sodium ion and compromise the utilization of active component at high rates, TSC still delivered and higher volume capacity under a current density of 1 A g^{-1}. When the current density was reduced back to 0.1 A g^{-1}, the discharging capacity of TSC recovered a high value of 343 mAh cm^{-3}, showing good reversibility. The decent high-rate performance of TSC could be attributed to the smaller charge transfer resistance (4.788 Ω) and diffusion resistance compared with TiO$_2$ (215 Ω) as revealed by the electrochemical impedance spectroscopy (Figure S5E), suggesting improved electronic/ionic transport in the heterostructured TSC particles as discussed shortly.

Figure 3E compares the cycling stability of TSC, porous TiO$_2$, and TS composite without carbon layer. The volumetric capacity of TSC was twice higher than that of TiO$_2$ and maintained a high value of 261 mAh cm^{-3} after 200 cycles at the current density of 200 mA g^{-1}, which is much higher than that of TS (135 mAh cm^{-3}) and TiO$_2$ (126 mAh cm^{-3}). The rapid capacity decay of TS might be related to the structural degradation of SnO$_2$ moieties upon repeated sodiation and poor stability of the electrode-electrolyte interface (Figure S5F).[52] The conformal carbon coating layer helps to improve the structural and interfacial stability of the TSC particles in the electrode, thus minimizing the capacity degradation. Compared with many reported anode materials for SIBs (Figure 3F and Table S1),[53–57] the TSC shows obvious advantages in terms of both gravimetric and volumetric capacity, which is of critical importance for high-energy SIBs.

To further investigate the charge storage kinetics in the heterostructure particles, the CV curves under different scanning rates were measured (Figure S6). To distinguish the origin of the capacity, the relationship between scan rate and peak current was fitted as follows:

$$i = av^b$$

$$\log(i) = b\log(v) + \log(a)$$

where a and b are adaptation parameters. In particular, $b = 0.5$ and 1 represent complete diffusion-controlled and complete pseudocapacitance contribution during the cycle, respectively. The dominant oxidation peak and corresponding reduction peak were selected from the CV curve for analysis. The b values of oxidation peak and reduction peak of TiO$_2$ electrode were 0.914 and 0.953, respectively (Figure 4A), suggesting pseudocapacitive charge storage behavior. As for the compact TSC particles, the b values still reached 0.821 and 0.834, which is slightly lower than that of TiO$_2$ and the stored charge is still dominated by the pseudocapacitive contribution (Figure 4B).

To quantify the effect of heterostructure of TSC on charge transfer kinetics, galvanostatic intermittent titration technique was performed to obtain the diffusion coefficient of Na ions (Figure S7). Considering the porous nature of electrode, surface area of active material obtained by N$_2$ adsorption was used to represent the electrochemical active area of the electrode. The diffusion coefficient of Na ions in TSC during sodiation and desodiation processes was at least 4–5 times higher than that of TiO$_2$ (Figures 4C and 4D). Therefore, Na ions transport in the bulk of TSC would be faster than that in pristine TiO$_2$. Considering that SnO$_2$ suffers from more sluggish reaction kinetics than TiO$_2$,[31–33] the obvious improvement on sodium ion diffusion coefficient could be attributed to the unique heterogeneous structure. Specifically, the heterogeneous interface between TiO$_2$ and SnO$_2$ might be conducive to rapid ion transport, while the *in situ* generated Sn species might improve the electronic conductivity in the particles. Though the compact structure of TSC would increase the average length of ion transport and reduce the contact area between electrolyte and active material, a proper heterogeneous structure would warrant fast charge transfer and reaction kinetics within the particles.

In summary, compact TSC nanoparticles composed of TiO$_2$ and SnO$_2$ was synthesized as anode materials for SIBs, which showed high capacity and high-rate performance. The proper heterogeneous structure formed between TiO$_2$ and SnO$_2$ would enhance the charge transfer within compact particles. TSC exhibits a 4–5 times higher diffusion coefficient for Na ions than that of porous TiO$_2$, and displayed twice higher than TiO$_2$ and commercial hard carbon in volumetric capacity. This work demonstrates a feasible design principle toward anode materials with high gravimetric and volumetric capacity for potential industrial applications.

Limitations of the study

The Na transport and phase transition behaviors in the heterogeneous structure lack direct experimental observation and theoretical analysis. The initial Coulombic efficiency of the compact TSC particles is
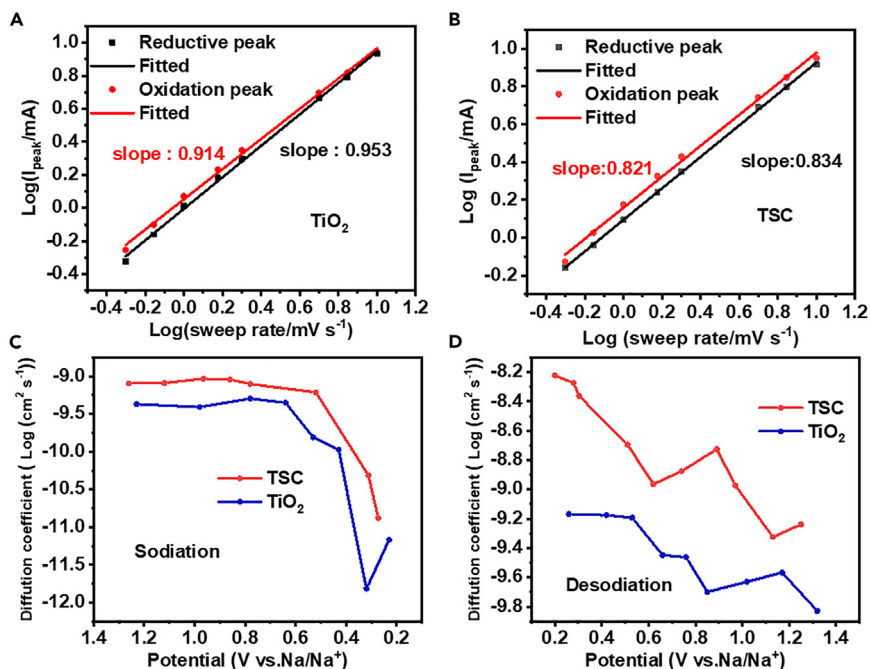
Figure 4. Electrochemical analysis of Na ions transport in TSC

(A–D) The *b* value analysis of (A) pristine TiO_2 and (B) TSC. Diffusion coefficients of TSC electrode and TiO_2 electrode at different potential during (C) sodiation (discharge) and (D) de-sodiation (charge) process.

relatively low, which demands additional Na compensation. The content of high-capacity component (SnO_2) is relatively low, limiting the capacity of TSC. Synthesis of the TSC involves multistep reactions and is less efficient.

STAR★METHODS

Detailed methods are provided in the online version of this paper and include the following:

- KEY RESOURCES TABLE
- RESOURCE AVAILABILITY
  - Lead contact
  - Materials availability
  - Data and code availability
- EXPERIMENTAL MODEL AND SUBJECT DETAILS
- METHOD DETAILS
  - Experimental section
  - Material characterization
  - Electrochemical tests

SUPPLEMENTAL INFORMATION

Supplemental information can be found online at https://doi.org/10.1016/j.isci.2023.106642.

AUTHOR CONTRIBUTIONS

Conceptualization: H.B.W. and Z.H.; Methodology: Z.H.; Investigation: Z.H., Z.C., and Q.L.; Writing – Original Draft: Z.H. and Z.C.; Writing – Review & Editing: H.B.W.; Funding Acquisition: H.B.W.

DECLARATION OF INTERESTS

There are no conflicts to declare.

REFERENCES

1. Zhao, L., and Qu, Z. (2022). Advanced flexible electrode materials and structural designs for sodium ion batteries. J. Energy Chem. 71, 108–128. https://doi.org/10.1016/j.jechem.2022.03.008.

2. Guo, Z., Qian, G., Wang, C., Zhang, G., Yin, R., Liu, W.-D., Liu, R., and Chen, Y. (2022). Progress in electrode materials for the industrialization of sodium-ion batteries. Prog. Nat. Sci.: Mater. Int. https://doi.org/10.1016/j.pnsc.2022.12.003.

3. Kumar, A., Nagmani, and Puravankara, S. (2022). Symmetric sodium-ion batteries—materials, mechanisms, and prospects. Mater. Today Energy 29, 101115. https://doi.org/10.1016/j.mtener.2022.101115.

4. Ud Din, M.A., Li, C., Zhang, L., Han, C., and Li, B. (2021). Recent progress and challenges on the bismuth-based anode for sodium-ion batteries and potassium-ion batteries. Mater. Today Phys. 21, 100486. https://doi.org/10.1016/j.mtphys.2021.100486.

5. Muhammed Hafiz, N.S., Singla, G., and Kumar Jha, P. (2022). Next generation sodium-ion battery: a replacement of lithium. Mater. Today Proc. https://doi.org/10.1016/j.matpr.2022.11.245.

6. Fatima, H., Zhong, Y., Wu, H., and Shao, Z. (2021). Recent advances in functional oxides for high energy density sodium-ion batteries. Mater. Rep. Energy 1, 100022. https://doi.org/10.1016/j.matre.2021.100022.

7. Ma, M., Zhang, S., Wang, L., Yao, Y., Shao, R., Shen, L., Yu, L., Dai, J., Jiang, Y., Cheng, X., et al. (2021). Harnessing the volume expansion of MoS3 anode by structure engineering to achieve high performance beyond lithium-based rechargeable batteries. Adv. Mater. 33, 2106232. https://doi.org/10.1002/adma.202106232.

8. Sun, Z., Li, M., Xiao, B., Liu, X., Lin, H., Jiang, B., Liu, H., Li, M., Peng, D.-L., and Zhang, Q. (2022). In situ transmission electron microscopy for understanding materials and interfaces challenges in all-solid-state lithium batteries. eTransportation 14, 100203. https://doi.org/10.1016/j.etran.2022.100203.

9. Xie, F., Zhang, L., Gu, Q., Chao, D., Jaroniec, M., and Qiao, S.-Z. (2019). Multi-shell hollow structured Sb2S3 for sodium-ion batteries with enhanced energy density. Nano Energy 60, 591–599. https://doi.org/10.1016/j.nanoen.2019.04.008.

10. Wang, Z., Feng, X., Bai, Y., Yang, H., Dong, R., Wang, X., Xu, H., Wang, Q., Li, H., Gao, H., and Wu, C. (2021). Probing the energy storage mechanism of quasi-metallic Na in hard carbon for sodium-ion batteries. Adv. Energy Mater. 11, 2003854. https://doi.org/10.1002/aenm.202003854.

11. Irisarri, E., Ponrouch, A., and Palacin, M.R. (2015). Review—hard carbon negative electrode materials for sodium-ion batteries. J. Electrochem. Soc. 162, A2476–A2482. https://doi.org/10.1149/2.0091514jes.

12. Xiao, L., Lu, H., Fang, Y., Sushko, M.L., Cao, Y., Ai, X., Yang, H., and Liu, J. (2018). Low-defect and low-porosity hard carbon with high coulombic efficiency and high capacity for practical sodium ion battery anode. Adv. Energy Mater. 8, 1703238. https://doi.org/10.1002/aenm.201703238.

13. Xie, F., Xu, Z., Guo, Z., and Titirici, M.-M. (2020). Hard carbons for sodium-ion batteries and beyond. Prog. Energy 2, 042002. https://doi.org/10.1088/2516-1083/aba5f5.

14. Ding, C., Huang, L., Lan, J., Yu, Y., Zhong, W.-H., and Yang, X. (2020). Superresilient hard carbon nanofabrics for sodium-ion batteries. Small 16, 1906883. https://doi.org/10.1002/smll.201906883.

15. Wang, H., Chen, H., Chen, C., Li, M., Xie, Y., Zhang, X., Wu, X., Zhang, Q., and Lu, C. (2023). Tea-derived carbon materials as anode for high-performance sodium ion batteries. Chin. Chem. Lett. 34, 107465. https://doi.org/10.1016/j.cclet.2022.04.063.

16. Yan, J., Li, H., Wang, K., Jin, Q., Lai, C., Wang, R., Cao, S., Han, J., Zhang, Z., Su, J., and Jiang, K. (2021). Ultrahigh phosphorus doping of carbon for high-rate sodium ion batteries anode. Adv. Energy Mater. 11, 2003911. https://doi.org/10.1002/aenm.202003911.

17. Peng, P.-P., Wu, Y.-R., Li, X.-Z., Zhang, J.-H., Li, Y.-W., Cui, P., and Yi, T.-F. (2021). Toward superior lithium/sodium storage performance: design and construction of novel TiO2-based anode materials. Rare Met. 40, 3049–3075. https://doi.org/10.1007/s12598-021-01742-z.

18. Lunell, S., Stashans, A., Ojamäe, L., Lindström, H., and Hagfeldt, A. (1997). Li and Na diffusion in TiO2 from quantum chemical theory versus electrochemical experiment. J. Am. Chem. Soc. 119, 7374–7380. https://doi.org/10.1021/ja9708629.

19. Kim, K.-T., Ali, G., Chung, K.Y., Yoon, C.S., Yashiro, H., Sun, Y.-K., Lu, J., Amine, K., and Myung, S.-T. (2014). Anatase titania nanorods as an intercalation anode material for rechargeable sodium batteries. Nano Lett. 14, 416–422. https://doi.org/10.1021/nl402747x.

20. Su, D., Dou, S., and Wang, G. (2015). Anatase TiO2: better anode material than amorphous and rutile phases of TiO2 for Na-ion batteries. Chem. Mater. 27, 6022–6029. https://doi.org/10.1021/acs.chemmater.5b02348.

21. Wu, L., Buchholz, D., Bresser, D., Gomes Chagas, L., and Passerini, S. (2014). Anatase TiO2 nanoparticles for high power sodium-ion anodes. J. Power Sources 251, 379–385. https://doi.org/10.1016/j.jpowsour.2013.11.083.

22. González, J.R., Alcántara, R., Nacimiento, F., Ortiz, G.F., and Tirado, J.L. (2014). Microstructure of the epitaxial film of anatase nanotubes obtained at high voltage and the mechanism of its electrochemical reaction with sodium. CrystEngComm 16, 4602–4609. https://doi.org/10.1039/C4CE00272E.

23. Wei, Q., Chang, X., Butts, D., DeBlock, R., Lan, K., Li, J., Chao, D., Peng, D.-L., and Dunn, B. (2023). Surface-redox sodium-ion storage in anatase titanium oxide. Nat. Commun. 14, 7. https://doi.org/10.1038/s41467-022-35617-3.

24. Zhao, B., Liu, Q., Chen, Y., Liu, Q., Yu, Q., and Wu, H.B. (2020). Interface-induced pseudocapacitance in nonporous heterogeneous particles for high volumetric sodium storage. Adv. Funct. Mater. 30, 2002019. https://doi.org/10.1002/adfm.202002019.

25. Zheng, Y., Zhou, T., Zhang, C., Mao, J., Liu, H., and Guo, Z. (2016). Boosted charge transfer in SnS/SnO2 heterostructures: toward high rate capability for sodium-ion batteries. Angew. Chem. Int. Ed. Engl. 55, 3408–3413. https://doi.org/10.1002/anie.201510978.

26. Fan, L., Li, X., Yan, B., Feng, J., Xiong, D., Li, D., Gu, L., Wen, Y., Lawes, S., and Sun, X. (2016). Controlled SnO2 crystallinity effectively dominating sodium storage performance. Adv. Energy Mater. 6, 1502057. https://doi.org/10.1002/aenm.201502057.

27. Patra, J., Chen, H.-C., Yang, C.-H., Hsieh, C.-T., Su, C.-Y., and Chang, J.-K. (2016). High dispersion of 1-nm SnO2 particles between graphene nanosheets constructed using supercritical CO2 fluid for sodium-ion battery anodes. Nano Energy 28, 124–134. https://doi.org/10.1016/j.nanoen.2016.08.044.

28. Wang, M., Wang, X., Yao, Z., Tang, W., Xia, X., Gu, C., and Tu, J. (2019). SnO2 nanoflake arrays coated with polypyrrole on a carbon cloth as flexible anodes for sodium-ion

batteries. ACS Appl. Mater. Interfaces 11, 24198–24204. https://doi.org/10.1021/acsami.9b08378.

29. Jin, X., Sheng, L., Jiang, L., Xiao, Z., Wang, D., Jiang, M., Lin, X., Zhang, X., Duan, X., and Shi, J. (2022). Manganese sulfate-derived α/γ-MnS embedded in N-doped layered carbon for high-performance lithium-ion batteries. Mater. Today Chem. 24, 100992. https://doi.org/10.1016/j.mtchem.2022.100992.

30. Wang, C., Sheng, L., Jiang, M., Lin, X., Wang, Q., Guo, M., Wang, G., Zhou, X., Zhang, X., Shi, J., and Jiang, L. (2023). Flexible SnSe2/N-doped porous carbon-fiber film as anode for high-energy-density and stable sodium-ion batteries. J. Power Sources 555, 232405. https://doi.org/10.1016/j.jpowsour.2022.232405.

31. Zhang, Y., Xie, J., Zhang, S., Zhu, P., Cao, G., and Zhao, X. (2015). Ultrafine tin oxide on reduced graphene oxide as high-performance anode for sodium-ion batteries. Electrochim. Acta 151, 8–15. https://doi.org/10.1016/j.electacta.2014.11.009.

32. Li, Z., Ding, J., Wang, H., Cui, K., Stephenson, T., Karpuzov, D., and Mitlin, D. (2015). High rate SnO2–Graphene Dual Aerogel anodes and their kinetics of lithiation and sodiation. Nano Energy 15, 369–378. https://doi.org/10.1016/j.nanoen.2015.04.018.

33. Wang, Y.-X., Lim, Y.-G., Park, M.-S., Chou, S.-L., Kim, J.H., Liu, H.-K., Dou, S.-X., and Kim, Y.-J. (2014). Ultrafine SnO2 nanoparticle loading onto reduced graphene oxide as anodes for sodium-ion batteries with superior rate and cycling performances. J. Mater. Chem. 2, 529–534. https://doi.org/10.1039/C3TA13592F.

34. Liang, J., Zhang, L., XiLi, D., and Kang, J. (2020). Rational design of hollow tubular SnO2@TiO2 nanocomposites as anode of sodium ion batteries. Electrochim. Acta 341, 136030. https://doi.org/10.1016/j.electacta.2020.136030.

35. Yang, L.Y., Xie, J.R., Abliz, A., Liu, J., Wu, R., Tang, S.S., Wang, S.Y., Wu, L.L., and Zhu, Y.Y. (2019). Hollow paramecium-like SnO2/TiO2 heterostructure designed for sodium storage. J. Solid State Chem. 274, 176–181. https://doi.org/10.1016/j.jssc.2019.03.032.

36. Tian, Y., Hu, P., Zhu, T., Liu, Z., Hu, G., Cai, C., Jian, Z., Zhou, L., and Mai, L. (2021). Three-layer structured SnO2@C@TiO2 hollow spheres for high-performance sodium storage. Energy Environ. Mater. 4, 428–433. https://doi.org/10.1002/eem2.12117.

37. Wang, L., Lin, C., Yang, G., Wang, N., and Yan, W. (2022). SnO2 nanosheets grown on in-situ formed N-doped branched TiO2/C nanofibers as binder-free anodes for sodium-ion storage. Electrochim. Acta 411, 140049. https://doi.org/10.1016/j.electacta.2022.140049.

38. Wu, X., Xia, S., Huang, Y., Hu, X., Yuan, B., Chen, S., Yu, Y., and Liu, W. (2019). High-performance, low-cost, and dense-structure electrodes with high mass loading for lithium-ion batteries. Adv. Funct. Mater. 29, 1903961. https://doi.org/10.1002/adfm.201903961.

39. Wu, H.B., Lou, X.W.D., and Hng, H.H. (2012). Synthesis of uniform layered protonated titanate hierarchical spheres and their transformation to anatase TiO2 for lithium-ion batteries. Chemistry 18, 2094–2099. https://doi.org/10.1002/chem.201102628.

40. Cheng, Y., Wang, S., Zhou, L., Chang, L., Liu, W., Yin, D., Yi, Z., and Wang, L. (2020). SnO2 quantum dots: rational design to achieve highly reversible conversion reaction and stable capacities for lithium and sodium storage. Small 16, 2000681. https://doi.org/10.1002/smll.202000681.

41. Ma, D., Li, Y., Mi, H., Luo, S., Zhang, P., Lin, Z., Li, J., and Zhang, H. (2018). Robust SnO2−x nanoparticle-impregnated carbon nanofibers with outstanding electrochemical performance for advanced sodium-ion batteries. Angew. Chem. Int. Ed. Engl. 57, 8901–8905. https://doi.org/10.1002/anie.201802672.

42. Gan, Q., He, H., Zhu, Y., Wang, Z., Qin, N., Gu, S., Li, Z., Luo, W., and Lu, Z. (2019). Defect-assisted selective surface phosphorus doping to enhance rate capability of titanium dioxide for sodium ion batteries. ACS Nano 13, 9247–9258. https://doi.org/10.1021/acsnano.9b03766.

43. Chen, X., Tian, J., Li, P., Fang, Y., Fang, Y., Liang, X., Feng, J., Dong, J., Ai, X., Yang, H., and Cao, Y. (2022). An overall understanding of sodium storage behaviors in hard carbons by an "adsorption-intercalation/filling" hybrid mechanism. Adv. Energy Mater. 12, 2200886. https://doi.org/10.1002/aenm.202200886.

44. Malibo, P.M., Makgwane, P.R., and Baker, P.G. (2021). Hetero-mixed TiO2-SnO2 interfaced nano-oxide catalyst with enhanced activity for selective oxidation of furfural to maleic acid. Inorg. Chem. Commun. 129, 108637. https://doi.org/10.1016/j.inoche.2021.108637.

45. Taucher, T.C., Hehn, I., Hofmann, O.T., Zharnikov, M., and Zojer, E. (2016). Understanding chemical versus electrostatic shifts in X-ray photoelectron spectra of organic self-assembled monolayers. J. Phys. Chem. C Nanomater. Interfaces 120, 3428–3437. https://doi.org/10.1021/acs.jpcc.5b12387.

46. Greczynski, G., and Hultman, L. (2020). X-ray photoelectron spectroscopy: towards reliable binding energy referencing. Prog. Mater. Sci. 107, 100591. https://doi.org/10.1016/j.pmatsci.2019.100591.

47. Bagus, P.S., Ilton, E.S., and Nelin, C.J. (2013). The interpretation of XPS spectra: insights into materials properties. Surf. Sci. Rep. 68, 273–304. https://doi.org/10.1016/j.surfrep.2013.03.001.

48. Nie, S., Liu, L., Liu, J., Xia, J., Zhang, Y., Xie, J., Li, M., and Wang, X. (2019). TiO2-Sn/C composite nanofibers with high-capacity and long-cycle life as anode materials for sodium ion batteries. J. Alloys Compd. 772, 314–323. https://doi.org/10.1016/j.jallcom.2018.09.044.

49. Wang, Y., Su, D., Wang, C., and Wang, G. (2013). SnO2@MWCNT nanocomposite as a high capacity anode material for sodium-ion batteries. Electrochem. Commun. 29, 8–11. https://doi.org/10.1016/j.elecom.2013.01.001.

50. Dirican, M., Lu, Y., Ge, Y., Yildiz, O., and Zhang, X. (2015). Carbon-confined SnO2-electrodeposited porous carbon nanofiber composite as high-capacity sodium-ion battery anode material. ACS Appl. Mater. Interfaces 7, 18387–18396. https://doi.org/10.1021/acsami.5b04338.

51. Huang, Z., Hou, H., Zou, G., Chen, J., Zhang, Y., Liao, H., Li, S., and Ji, X. (2016). 3D porous carbon encapsulated SnO2 nanocomposite for ultrastable sodium ion batteries. Electrochim. Acta 214, 156–164. https://doi.org/10.1016/j.electacta.2016.08.040.

52. Gu, M., Kushima, A., Shao, Y., Zhang, J.-G., Liu, J., Browning, N.D., Li, J., and Wang, C. (2013). Probing the failure mechanism of SnO2 nanowires for sodium-ion batteries. Nano Lett. 13, 5203–5211. https://doi.org/10.1021/nl402633n.

53. Xie, X., Zhao, M.-Q., Anasori, B., Maleski, K., Ren, C.E., Li, J., Byles, B.W., Pomerantseva, E., Wang, G., and Gogotsi, Y. (2016). Porous heterostructured MXene/carbon nanotube composite paper with high volumetric capacity for sodium-based energy storage devices. Nano Energy 26, 513–523. https://doi.org/10.1016/j.nanoen.2016.06.005.

54. Wang, X., Kajiyama, S., Iinuma, H., Hosono, E., Oro, S., Moriguchi, I., Okubo, M., and Yamada, A. (2015). Pseudocapacitance of MXene nanosheets for high-power sodium-ion hybrid capacitors. Nat. Commun. 6, 6544. https://doi.org/10.1038/ncomms7544.

55. Beda, A., Rabuel, F., Morcrette, M., Knopf, S., Taberna, P.-L., Simon, P., and Matei Ghimbeu, C. (2021). Hard carbon key properties allow for the achievement of high Coulombic efficiency and high volumetric capacity in Na-ion batteries. J. Mater. Chem. A Mater. 9, 1743–1758. https://doi.org/10.1039/D0TA07687B.

56. Ding, J., Wang, H., Li, Z., Cui, K., Karpuzov, D., Tan, X., Kohandehghan, A., and Mitlin, D. (2015). Peanut shell hybrid sodium ion capacitor with extreme energy–power rivals lithium ion capacitors. Energy Environ. Sci. 8, 941–955. https://doi.org/10.1039/C4EE02986K.

57. Zhang, J., Lv, W., Tao, Y., He, Y.-B., Wang, D.-W., You, C.-H., Li, B., Kang, F., and Yang, Q.-H. (2015). Ultrafast high-volumetric sodium storage of folded-graphene electrodes through surface-induced redox reactions. Energy Storage Mater. 1, 112–118. https://doi.org/10.1016/j.ensm.2015.08.006.

STAR★METHODS

KEY RESOURCES TABLE

REAGENT or RESOURCE	SOURCE	IDENTIFIER
Chemicals, peptides, and recombinant proteins		
Super Carbon	SCRC	CAS:1333-86-4
$C_4H_{11}NO_3 \cdot HCl$	SCRC	CAS:6850-28-8
$SnCl_2 \cdot 2H_2O$	SCRC	CAS:10025-69-1
$C_{16}H_{36}O_4Ti$	SCRC	CAS:5593-70-4
C_3H_7NO (DMF)	Sigma-Aldrich	CAS:68-12-2
C_5H_9NO (NMP)	Sigma-Aldrich	CAS:872-50-4
C_2H_5OH	SCRC	CAS: 64-17-5
$C_8H_{12}ClNO_2$	SCRC	CAS:62-31-7
HCl	SCRC	CAS:7647-01-0
$C_2H_2F_2$ (PVDF)	DODOCHEM	CAS: 24937-79-9
Software and algorithms		
Origin 2018	Electronic Arts Inc	https://www.originlab.com/
MS Office 2016	Microsoft	https://www.microsoft.com/zh-cn/microsoft-365/microsoft-office
EC-Lab	Bio-Logic	https://www.biologic.net/support-software/ec-lab-software/
BTSDA	Neware	https://neware.com.cn/BTS

RESOURCE AVAILABILITY

Lead contact
Further information and requests for resources and reagents should be directed to and will be fulfilled by the lead contact, Hao Bin Wu (hbwu@zju.edu.cn).

Materials availability
This study did not generate new unique materials.

Data and code availability
- All data reported in this paper will be shared by the lead contact upon request.
- There is no original code associated with this work.
- Any additional information required to reanalyze the data reported in this paper will be available from the lead contact upon request.

EXPERIMENTAL MODEL AND SUBJECT DETAILS
Our study does not use experimental models.

METHOD DETAILS
Identifiers of the reagents used in this work are given in key resources table.

Experimental section
Preparation of TiO2@SnO2
Firstly, 16.7 ml of N, N-dimethylformamide (DMF) and 50 ml of isopropyl alcohol (IPA) were thoroughly mixed in a 100 ml Teflon liner, followed by adding 1.67 ml of terabutyl titanate (TBT). The Teflon liner was then sealed in an autoclave and heated at 180°C for 20 hours. After cooling to room temperature,

the product was isolated by centrifugation, washed with ethanol, and dried at 80°C overnight. The precipitation was heated at 450°C under air for 2 hours at a heating rate of 2°C min^{-1} to obtain the pristine TiO_2.

Then, 100 mg of TiO_2 was dispersed to 50 ml of ethanol (C_2H_5OH) by ultrasonication for 30 minutes. 50 mg of stannous chloride dihydrate ($SnCl_2 \cdot 2H_2O$) was added to the above mixture and stirred for 10 minutes until fully dissolved. The obtained solution was heated in a water bath and stirred at 80°C until solvent was evaporated completely to obtain the $TiO_2@SnCl_2 \cdot 2H_2O$. The product was heated at 600°C for 5 hours under air at the heating rate of 2°C min^{-1} to obtain $TiO_2@SnO_2$ (denoted as TS). The SnO_2 sample was fabricated from $SnCl_2 \cdot 2H_2O$ via the same heating method.

Preparation of TSC composite

Tris-HCl buffer solution was firstly prepared by dissolved 605.7 mg of Tris in 50 ml water, followed by slowly adding HCl solution until pH = 8.5. 100 mg of TS was then added to the above Tris-HCl buffer solution and sonicated for 30 min. Then, 25 mg of dopamine hydrochloride (HDA) were added into the above solution and stirred at 30°C for 24 hours. The precipitates were collected by centrifugation, washed with water and ethanol alternately, then dried at 80°C. The as-prepared products were annealed at 600°C for 5 hours at a heating rate of 5°C min^{-1} under Ar atmosphere to obtain TSC.

Material characterization

The structures of the materials were characterized by powder X-ray diffraction analysis (XRD, EMPYREAN PANalytical) with Cu Kα (λ=1.54 Å) radiation. The morphologies of the composites were examined via scanning electron microscopy (SEM) (Phenom LE) and transmission electron microscopy (TEM, HT770 120 kV). To identify their chemical status, X-ray photoelectron spectroscopy (XPS, Thermo Scientific K-Alpha) with an Al Kα excitation source was employed. The specific surface area and pore size distribution of the products were measured using the Brunauer-Emmett-Teller analyzer (BET) at 575 K (Micromeritics ASAP 2460).

Electrochemical tests

The TSC, acetylene black, and polyvinylidene fluoride (PVDF) were mixed in N-methyl pyrrolidone (NMP) solvent with a mass ratio of 8:1:1 to form uniform slurry. The slurry was then coated onto copper foil evenly, and then dried in vacuum oven at 75°C for 10 hours. The electrode films were punched into disks with a diameter of 12 mm. The typical mass loading of active material was 1.5-2 mg cm^{-2}.

The CR2032 half cells were assembled in argon-filled glove box with glass fiber (Whatman, GF/A) as separator, sodium foil as the counter electrode, and 130 µl of liquid electrolyte for each cell (1 M NaPF$_6$ in DME). The galvanostatic charge/discharge tests were conducted in a battery testing system (Neware BLC-300) with potential range of 0.01-2.50 V (vs Na/Na$^+$). The specific capacity was calculated based on the total weight of the TSC composite. Cyclic voltammetry (CV) was performed with scan rates of 0.1 mV s^{-1} and voltage range of 0.01–2.50 V (vs Na/Na$^+$) on an electrochemical workstation (Biologic). Electrochemical impedance spectra (EIS) test was performed with the frequency range from 20 kHz to 16 mHz on the same workstation.

The diffusion coefficient of TiO_2 and TSC electrodes were calculated based on the galvanostatic intermittent titration technique (GITT) profiles through Fick's second law. When the applied current is small and current pulse is short enough, the formula will be simplified to this following equation:

$$D = (4/(\pi \times \tau))(N_m \times V_m/S)^2(\Delta E_S/\Delta E_t)^2$$

where τ stands for the duration of the current pulse, N_m represents the electrode active molar quantity, V_m stands for the molar volume, S is the surface area of the electrode, ΔE_S represents the quasi-thermodynamic equilibrium potential difference before and after the current pulse, and ΔE_t is the potential difference during current pulse. The GITT test was performed via applying current pulses (0.1 A g^{-1}) with a pulse duration of 5 min and a relaxation process of 180 min for the first cycle and 240 min for the rest. The profiles collected in the second cycle were used for the analysis.